Numerical Study of the Influence of the Cross-Section Slenderness on the Rotational Capacity of Wide-Flange Steel Sections

Julien Richard[1], Elsy Saloumi[2], Joanna Nseir[3], Marielle Hayeck[4], Nicolas Boissonnade[5]

Abstract

The present paper focuses on the rotational capacity of H-shaped steel sections; in particular, the influence of local buckling is accounted for by means of a generalized cross-sectional slenderness, which is used as a new parameter to characterize the cross-sectional rotational capacity, and, by extension, the available deformation capacity.

Careful shell modelling of wide flange beams in bending was used in extensive F.E. parametric studies that included many parameters such as various materials (up to high strength steel), load and support arrangements, length-to-height ratios and web/flange slenderness. Specific attention was paid to the introduction of initial geometrical (local) imperfections.

The paper then analyzes the numerical results and points out the various influences of shear, moment gradient, yield stress, static system and length-to-height ratio on the available rotational capacity. In a second step, the rotational capacity demand vs. stability criterion is detailed, and related to the proposed generalized cross-sectional slenderness, which is shown to be more appropriate than the b/t ratios usually proposed in design codes. Finally, suggestions for new ways of allowing for plastic analysis through such approaches are given.

1. Introduction

The present paper is related to the rotational capacity of wide-flange, open section members; the intention is here to investigate new ways of defining the possibility to resort to a plastic analysis in practical design. These developments take place in the context of the development of the Overall Interaction Concept (O.I.C.) (Boissonnade 2013). The O.I.C., among other things, is meant to remove the preliminary "cross-section classification" design step, i.e. the classification of the cross-section into the plastic (so-called "class 1" in European standards Eurocode 3), compact (class 2), semi-compact (class 3) or slender range (class 4). This is achieved within the O.I.C. through the definition of a generalized cross-section slenderness $\lambda_{rel,CS}$ and of associated cross-section interaction curves that lead to a smooth and continuous definition of cross-sectional resistance, from plastic to slender capacity. Consequently, the classification step becomes

---

[1] MSc., University of Applied Sciences of Western Switzerland, <julien.richard@alumni.hes-so.ch>
[2] Graduate Student, University of Applied Sciences of Western Switzerland, <elsysaloumi @gmail.com>
[3] Graduate Student, University of Applied Sciences of Western Switzerland, <joanna.nseir@gmail.com>
[4] Graduate Student, University of Applied Sciences of Western Switzerland, <marielle_hayeck@hotmail.com>
[5] Professor, University of Applied Sciences of Western Switzerland, <nicolas.boissonnade@hefr.ch>

obsolete and disappears in the O.I.C. approach, avoiding many practical difficulties, inaccuracies and inconsistencies (Boissonnade 2013).

With the disappearance of the classification system, the criterion allowing the designer to perform a plastic analysis (formerly allowed for class 1 sections) vanishes as well. Therefore, the need to "re-introduce" such a criterion is clear and is dealt with in present paper. It may be added here that in daily practice, plastic design is quite popular in the U.K. and North America, so that clear procedures and recommendations are essential.

The basic idea developed in the present paper consists in an extended use of the $\lambda_{rel,CS}$ factor to define two families of sections:
- sections allowing for plastic analysis and design ("class 1" sections, possessing sufficient rotational capacity for a plastic failure mechanism to develop);
- other sections for which the extent of local buckling precludes the attainment of sufficient ductile deformation for the development of a plastic mechanism, so that plastic analysis is to be avoided.

In other words, this paper addresses the possibility to define limit values of $\lambda_{rel,CS}$ as a function of key parameters so as to replace the R_{dem} vs. R_{cap} criterion (see Fig. 1), where R_{dem} is the rotation demand and R_{cap} is the rotation capacity.

Figure 1: criterion to allow for plastic analysis
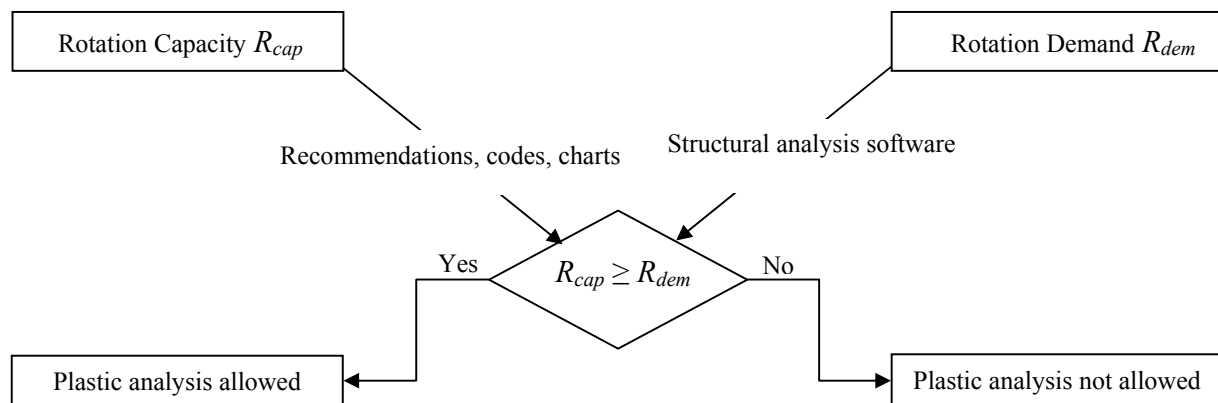
In this respect, a numerical strategy was developed, aiming at characterizing numerically both the demand and the cross-section rotational capacity. Expected leading parameters such as section slenderness, shear, yield strength, L/h ratio… were investigated separately through various static configurations and load definitions.

Section 2 first describes specific insights in the "$R_{stab,CS}$" parameter, which has the key role in the definition of $\lambda_{rel,CS}$ for the situation considered here. Section 3 then details the shell F.E. models used herein, and the associated parametric studies. Last, section 4 investigates the results of a sensitivity study to various parameters and properties, and relates R_{cap} to R_{dem} for a series of continuous beams situations.

2. Determination of $R_{STAB,CS}$

2.1. Nature and importance of $R_{STAB,CS}$ – Parametric studies

As already explained, the rotation capacity is here related to the overall cross-section relative slenderness $\lambda_{rel,CS}$ (Eq. 1); R_{RESIST} represents the factor (often also denoted as "load ratio") by which the initial loading has to be multiplied to reach the resistance limit, and $R_{STAB,CS}$ is the load ratio needed to reach the buckling load (local instability) of the ideal, elastic cross-section (so-called Linear Buckling Analysis) (Boissonnade 2013).

$$\lambda_{rel,CS} = \sqrt{\frac{R_{RESIST}}{R_{STAB,CS}}} \qquad (1)$$

This overall relative slenderness is a key parameter in the present study, and the current section focuses on a numerical calculation of $R_{STAB,CS}$. Its determination has been computed by means of CUFSM and FINELg software for comparison and validation; the numerical results obtained from both sources are presented, compared and discussed below.

In this preliminary study, two base profiles, an IPE500 S355 and an HEB300 S355 have been considered, loaded either in compression or under major-axis bending. For each cross-section dimensions, in order to cover all cross-sectional behavioral classes ranging from plastic to slender, the thickness of the web and flanges of these profiles were modified while their heights and width were kept constant. New section geometries (modified b/t ratios) were back-calculated from $\lambda_{rel,p}$ limits between classes (see Fig. 2). The $\lambda_{rel,p}$ limit values were set to 0.5 for the class 1-2 border and to 0.6 for the class 2-3 border (CEN 2005). As for the class 3 and 4 border, (elastic) limits have been based on the well-known Winter formulae (Johansson 2007).
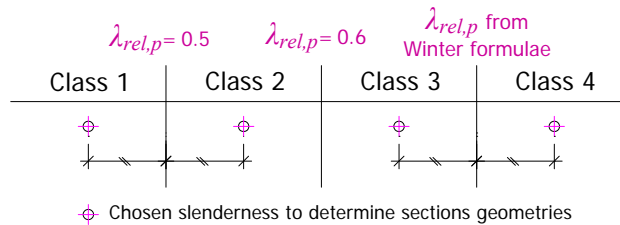

Figure 2: method used for the calculation of section geometries

The base sections have then been degenerated into various geometries, through a two-step procedure. In a first step, only the thickness of the most slender element was modified – into cases covering plastic to slender situations – while the other thickness was kept constant. In a second step, all thicknesses were modified proportionally. For the IPE500, web buckling usually occurs first, so that the first step consisted in modifying the web thickness while the flange thickness remained constant; then, web and flange thickness were varied simultaneously. As for the HEB300, where the flanges are rather sensitive to instabilities, flange thickness where modified and web thickness kept constant; then, web and flange thickness were varied proportionally.

2.2. Determination of $R_{STAB,CS}$ with CUFSM

A first sensitivity study was carried out with CUSFM to validate the density of the adopted meshes. Different meshes were tested and Table 1 reports on the number of elements used in flanges and webs within the different meshes. The number of elements in the flanges and webs was chosen in order to have equal strip widths (see Fig. 3). The meshes are varied from coarse to very dense, mesh f3 being the intermediate one.

Table 1: Various mesh refinement adapted in CUFSM

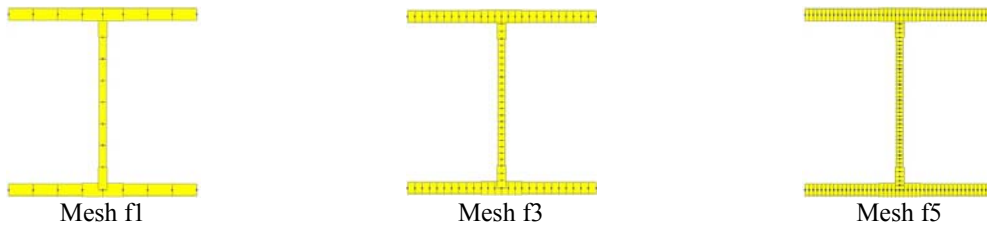|	IPE 500			HEB 300		
	Mesh f1	Mesh f3	Mesh f5	Mesh f1	Mesh f3	Mesh f5
Number of elements in flange n_f	6	22	38	8	26	46
Number of elements in web n_w	18	66	114	8	26	46

Figure 3: HEB300 meshing in CUFSM

As Fig. 4 clearly shows, the various minimum $R_{STAB,CS}$ values obtained by means of CUFSM indicate that mesh f1 is already sufficient to reach reliable $R_{STAB,CS}$ values, whatever the geometry or type of loading.
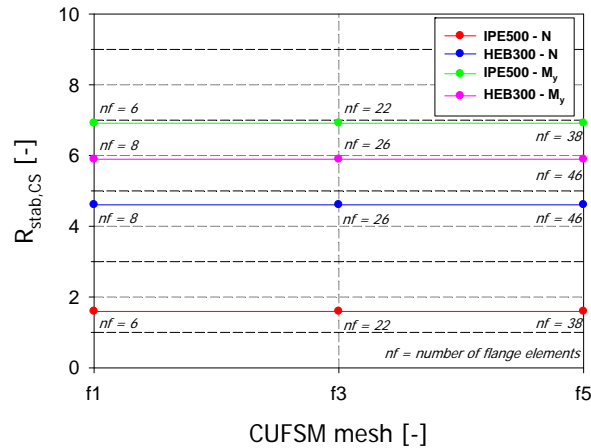

Figure 4: CUFSM results as a function of meshing refinement

Besides, specific attention was paid to the geometrical definition and modelling of the H-shaped section, especially towards the web-to-flange zone and flange radius area – CUFSM does not explicitly allow the modeling of fillets. In the case of hot-rolled profiles, owing to relatively stocky geometries, the influence of this zone can affect the results. Thus, for a correct representation of the section geometry and properties, both the fillets and the "overlapping area" were modeled by increasing the web and flange thickness in the radius area, as shown in Fig. 5, so that the increased thickness is equal to the corner region minus the overlapping area.
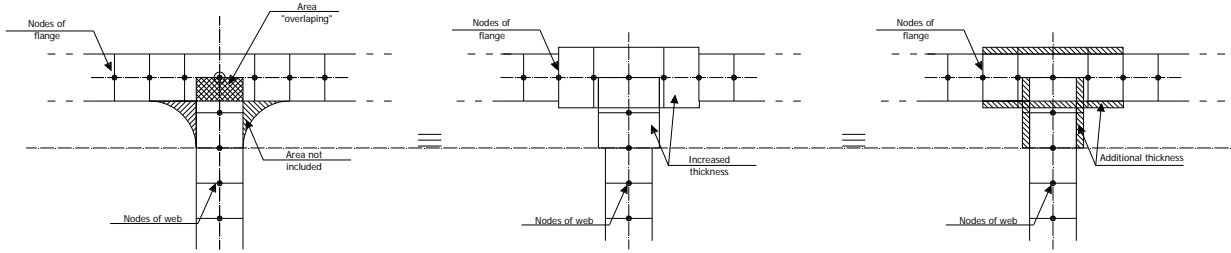
Figure 5: Accounting for flange radius in H-shaped cross-section in CUFSM modelling

A sub-study was carried out to investigate the influence of the additional thicknesses in the model on $R_{STAB,CS}$ values. Sections were considered under compression and major-axis bending only. Both models, without particular treatment of the web-to-flange junction area and models modified as explained above, were considered. In order to provide a fair comparison between models – they exhibit different cross-section properties –, identical initial loading was considered for all cases and reference was made to the models with extra thickness.

As Fig. 5 shows[6], non-negligible differences between the two models can be reported. As expected, the models with increased thickness were systematically exhibiting higher $R_{STAB,CS}$ values; this is easily explained by the fact that these models possess a relatively larger area and because local buckling (governing cross-section buckling mode here) develops with reduced buckling widths, thus leading to higher critical stresses, i.e. $R_{STAB,CS}$ factors. Therefore, in the following, the more sophisticated model with increased thickness was kept as reference. In some cases (see Fig. 6b), the buckling mode leading to the minimum $R_{STAB,CS}$ even changed from local to distortional.
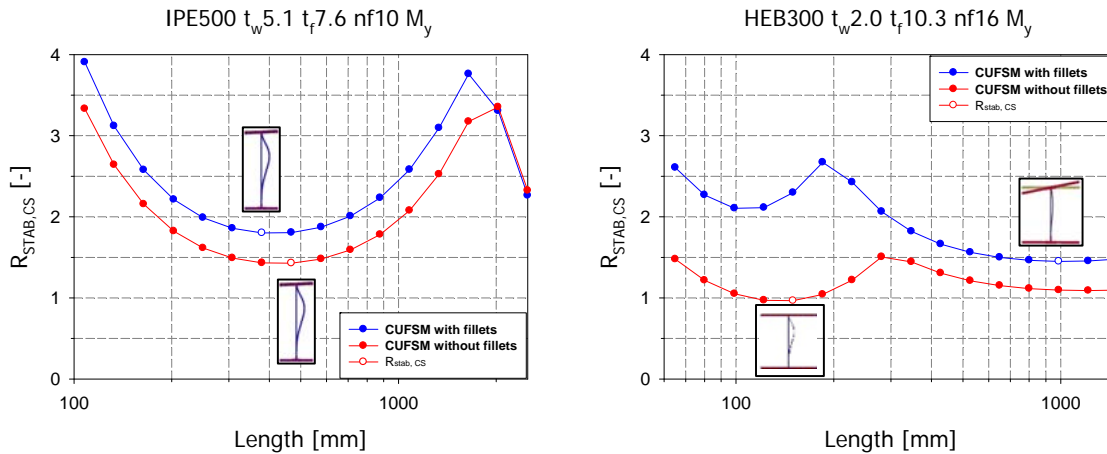

Figure 6: Examples of results from the two different CUFSM models with respect to fillets modelling

Table 2 and 3 report a series of results obtained for compression and major-axis bending load cases, respectively. Sections in compression are seen to be less sensitive to the modelling of the radius zone. However, as a general tendency, the differences between the two models prediction increase with cross-section slenderness. The maximum deviations recorded are: 11% for class 1, 18% for class 2, 21% for class 3, and 33% for class 4. It is to be mentioned too that such models exhibit geometrical static properties in close agreement with the real properties of the section.

---

[6] Buckling mode 1 was considered for comparison purposes.

Table 2: CUFSM results for sections under compression

Axial Force N	IPE500_tf16_tw24*	IPE500_tf16_tw17	IPE500_tf16_tw14.5	**IPE500_tf16_tw10.2**	IPE500_tf9.0_tw17	IPE500_tf7.6_tw14.5	IPE500_tf6.7_tw10.2
Web	class 1	class 2	class 3	**class 4**	class 2	class 3	class 4
Flange	class 1	class 1	class 1	**class 1**	class 2	class 3	class 4
$R_{stab,\ CS\ (with\ filets)}$	-	3.13	2.56	**1.59**	2.50	1.87	1.02
$R_{stab,\ CS\ (without\ filets)}$	4.98	3.06	2.47	**1.46**	2.37	1.73	0.90
Difference [%]	-	-2.2	-3.6	**-7.8**	-5.1	-7.3	-12
Buckled shape with an increased thickness in the radius area							
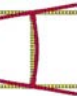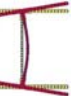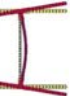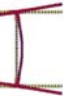
Axial Force N	**HEB300_tf19_tw11**	HEB300_tf14.4_tw11	HEB300_tf12_tw11	HEB300_tf10.3_tw11	HEB300_tf14.4_tw8.6	HEB300_tf12_tw7.6	HEB300_tf10.3_tw6.9
Web	**class 1**	class 1	class 1	class 1	class 2	class 3	class 4
Flange	**class 1**	class 2	class 3	class 4	class 2	class 3	class 4
$R_{stab,\ CS\ (with\ filets)}$	**4.62**	3.08	2.45	2.07	2.78	2.04	1.59
$R_{stab,\ CS\ (without\ filets)}$	**4.21**	2.68	2.06	1.67	2.39	1.68	1.25
Difference [%]	**-8.8**	-13	-16	-19	-14	-18	-21
Buckled shape with an increased thinckness in the radius area							

Table 3: CUFSM results for sections under major-axis bending

Moment M_y	**IPE500_tf16_tw10.2**	IPE500_tf16_tw6.9	IPE500_tf_16_tw5.1	IPE500_tf16_tw3.7	IPE500_tf9.0_tw6.9	IPE500_tf7.6_tw5.1	IPE500_tf6.7_tw3.7
Web	**class 1**	class 1	class 1	class 1	class 2	class 3	class 4
Flange	**class 1**	class 2	class 3	class 4	class 2	class 3	class 4
$R_{stab,\ CS\ (with\ filets)}$	**6.93**	4.90	2.94	1.65	2.66	1.80	1.28
$R_{stab,\ CS\ (without\ filets)}$	**6.51**	4.19	2.36	1.25	2.24	1.43	0.96
Difference [%]	**-6.0**	-15	-20	-24	-16	-21	-25
Buckled shape with an increased thinckness in the radius area							

Moment M_y	**HEB300_tf19_tw11**	HEB300_tf14.4_tw11	HEB300_tf12_tw11	HEB300_tf10.3_tw11	HEB300_tf14.4_tw3.5	HEB300_tf12_tw2.7	HEB300_tf10.3_tw2
Web	**class 1**	class 2	class 3	class 4	class 2	class 3	class 4
Flange	**class 1**	class 1	class 1	class 1	class 2	class 3	class 4
$R_{stab,\ CS\ (with\ filets)}$	**5.90**	3.97	3.14	2.58	2.78	1.95	1.45
$R_{stab,\ CS\ (without\ filets)}$	**5.22**	3.35	2.55	2.03	2.28	1.54	0.966 (1.09)
Difference [%]	**-11**	-16	-19	-21	-18	-21	-33 (-25)
Buckled shape with an increased thinckness in the radius area							

*: No increased thickness in the web-to-flanges junction was made due to the section geometry
In bold: original cross-section dimensions

2.3. Determination of $R_{STAB,CS}$ with FINELg

Prior to investigating the numerical determination of $R_{STAB,CS}$ by means of shell models, numerical tests on mesh refinement were also performed. Non-linear F.E.M. software FINELg (2012), continuously developed at the University of Liège and Greisch Engineering Office since 1970, was used. As a general basis, the longitudinal mesh was chosen so as to use square shell elements; the different meshes tested are shown in Table 4[7]. All results detailed hereafter have been obtained on short members ($L = 0.5\,h$ to $5\,h$, h being the height of the cross-section considered) to capture local buckling only. The use of kinematic linear constraints has been made between flange and web nodes and ideal "fork conditions" were adopted. Loading has been implemented at the member's end by means of suitable distributions of concentrated forces at the flanges tips, given the kinematics constraints (see Fig. 8).

Table 4: FINELg investigated meshes

	IPE500				HEB300			
	Mesh 1	Mesh 2	Mesh 3	Mesh 4	Mesh 1	Mesh 2	Mesh 3	Mesh 4
Number of elements in flange n_f	6	8	10	12	10	12	16	18
Number of elements in web n_w	18	24	30	36	10	12	16	18

$n_f = 6$ $n_f = 8$ $n_f = 10$ $n_f = 12$
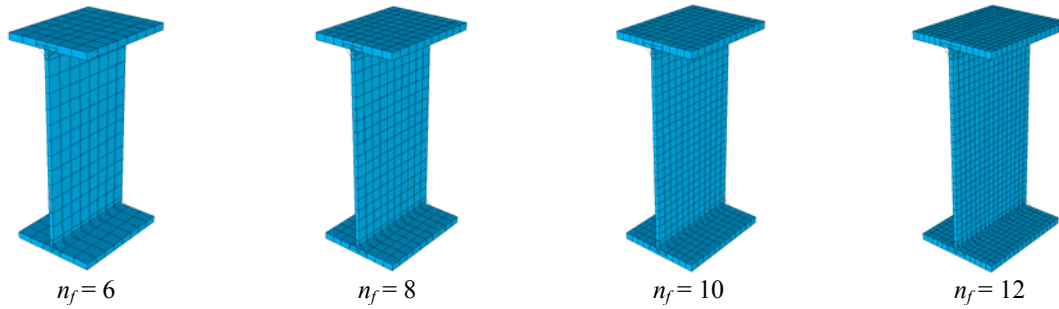
Figure 7: Various HEB300 meshes in FINELg
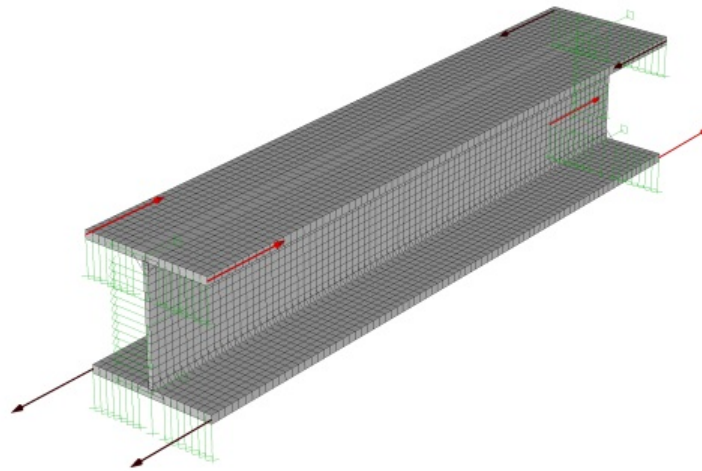
Figure 8: Loading and support conditions for major-axis bending

---

[7] Meshes were defined according to the flange and have equal length in all directions.

7

Fig. 9 gives an example of the obtained results. Two different load cases have been considered as well: axial compression N only, and constant major-axis bending moment M. $R_{STAB,CS}$ critical load ratios are reported versus the number of elements in the flanges (it is to be noted that the number of elements in the webs was adapted so as to keep similar shell elements widths between flanges and web, see for example in Fig. 7). As can be seen, mesh density n°3 leads to satisfactory results and was adopted in the following calculations.
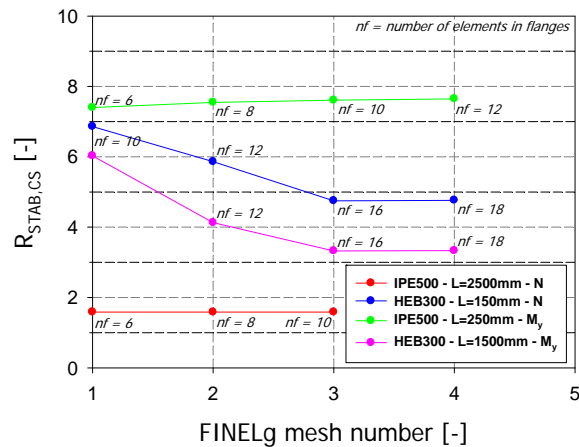
Figure 9: Influence of mesh refinement in FINELg models

The shell F.E. model was developed so as to fit the real geometrical properties of the members as closely as possible. Consequently, an additional square beam element was placed in the flange radius zone to account for the presence of the fillets and the overlapping area at the webs to flange junction which, without specific treatment, is usually counted twice in shell modelling of open sections. Also, an additional truss system has been implemented in the model to keep the flange radius zones unaffected by the extent of local buckling (Fig. 10).
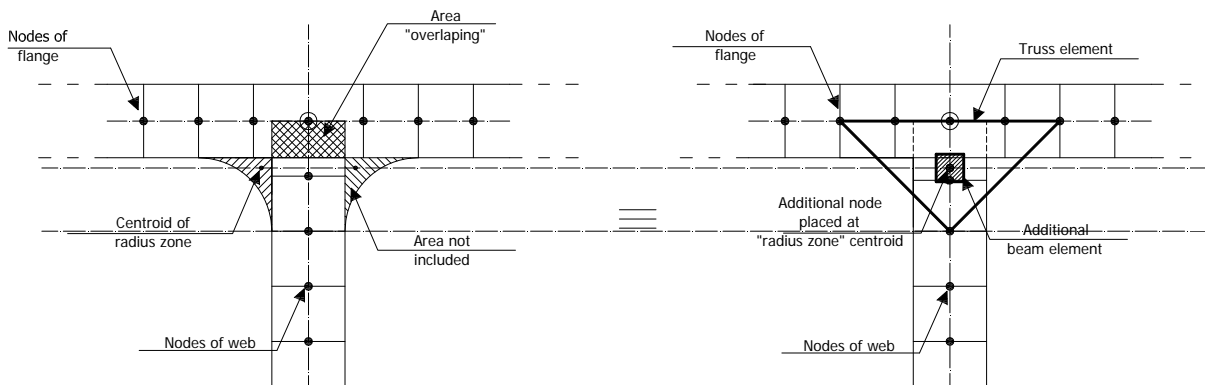
Figure 10: Accounting for flange radius in H-shaped cross-section in FINELg modelling

All modelling possibilities with respect to the treatment of the radius zone were tested in order to visualize the effect of one component (i.e. flanges or web) on the cross-section response. Fig. 11 gives graphical examples of the obtained results for an IPE500 and an HEB300 under constant bending moment. The general trend observed is a "vertical shift in $R_{STAB,CS}$" values, from little to moderate. Moreover, similarly to trends observed with a CUFSM modelling for the particular

case of the HEB300 with exaggerated slender web and flanges, the buckling mode changes from one type (local) to another one (distortional), see Fig. 11b.
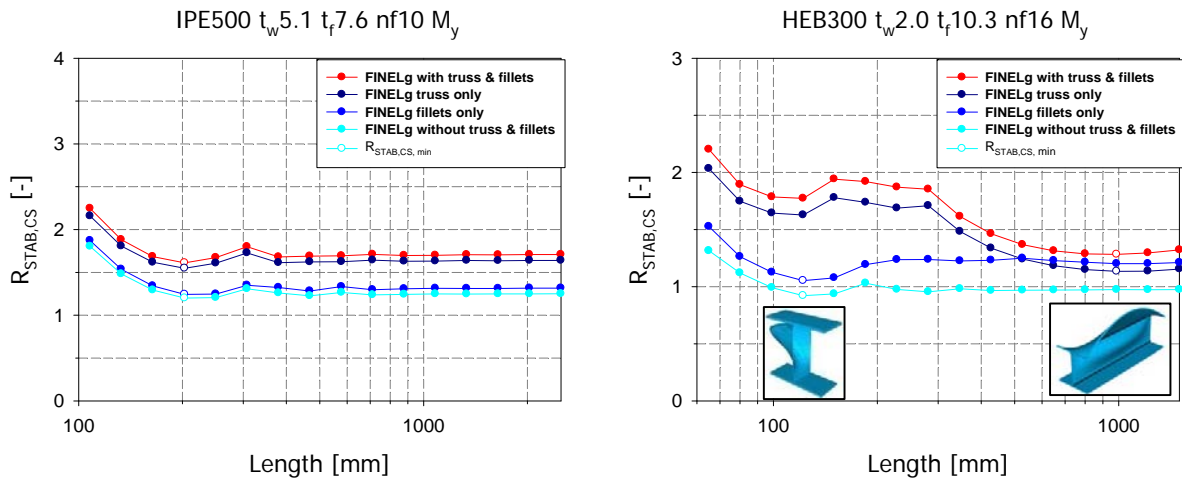
Figure 11: Examples of results for various FINELg F.E. models with respect to web-to-flange zone

Tables 5 and 6 report on the obtained results regarding both $R_{STAB,CS}$ minimum values and the relative differences with results obtained through F.E. models with an additional beam and truss system (T = Truss, B = additional Beam element). As expected, the largest difference is reached with the model without a truss or additional beam element, as being the softer model (identical initial loading was considered for all models making the load ratios $R_{STAB,CS}$ consistent and comparable). The case of an IPE500, where buckling of the cross-section is governed by web instability, is the most sensitive to the presence of the truss, owing to the difference in stiffness between its web and flanges. Also, following different flange/web relative local stiffness, the buckled shapes associated to the minimum $R_{STAB,CS}$ values may qualitatively change, as highlighted by the red frames in Table 6.

For the HEB300 case mainly governed by flange instability, the presence of the truss has more influence than that of the additional beam element[8]. The maximum observed deviations per cross-sections classes are the following: class 1: 13%, class 2: 24%, class 3: 27%, and class 4: 31%. Therefore, as these modelling details are seen to have important influence on the results, both the truss system and the additional square beam element were kept for the consecutive F.E. studies.

---

[8] Flange fillets were kept constant.

Table 5: FINELg results for sections under compression

Axial Force N	IPE500_tf16_tw24*	IPE500_tf16_tw17	IPE500_tf16_tw14.5	IPE500_tf16_tw10.2	IPE500_tf9.0_tw17	IPE500_tf7.6_tw14.5	IPE500_tf6.7_tw10.2
$R_{stab,CS}$ (T&B)	-	3.03	2.50	**1.60**	2.36	1.73	0.92
$R_{stab,CS}$ (T only)	4.86	3.01	2.47	**1.57**	2.31	1.68	0.87
Difference [%]	-	-0.7	-1.1	**-1.9**	-2.0	-3	-6
$R_{stab,CS}$ (B only)	4.81	2.96	2.39	**1.41**	2.35	1.73	0.92
Difference [%]	-	-2.4	-4.3	**-12**	-0.5	-0.2	-0.04
$R_{stab,CS}$(noT&B)	4.81	2.94	2.37	**1.38**	2.49	1.67	0.87
Difference [%]	-	-3.1	-5.3	**-14**	5.5	-3.3	-5.7
Buckled shape with truss and additional beam element							

Axial Force N	HEB300_tf19_tw11	HEB300_tf14.4_tw11	HEB300_tf12_tw11	HEB300_tf10.3_tw11	HEB300_tf14.4_tw8.6	HEB300_tf12_tw7.6	HEB300_tf10.3_tw6.9
$R_{stab,CS}$ (T&B)	**4.40**	2.87	2.26	1.90	2.57	1.85	1.42
$R_{stab,CS}$ (T only)	**4.26**	2.72	2.11	1.75	2.42	1.69	1.26
Difference [%]	**-3.2**	-5.1	-6.7	-8.2	-6.0	-9	-11
$R_{stab,CS}$ (B only)	**4.31**	2.79	2.18	1.79	2.52	1.81	1.38
Difference [%]	**-2.1**	-2.9	-3.6	-5.9	-2.0	-1.9	-2.1
$R_{stab,CS}$(noT&B)	**4.17**	2.65	2.04	1.65	2.37	1.66	1.24
Difference [%]	**-5.3**	-7.7	-9.7	-13	-7.8	-10	-13
Buckled shape with truss and additional beam element							

Table 6: FINELg results for sections under major-axis bending.

Moment M_y	IPE500_tf16_tw10.2	IPE500_tf16_tw6.9	IPE500_tf_16_tw5.1	IPE500_tf16_tw3.7	IPE500_tf9.0_tw6.9	IPE500_tf7.6_tw5.1	IPE500_tf6.7_tw3.7
$R_{stab,CS}$ (T&B)	**6.61**	5.18	3.01	1.61	2.40	1.59	1.12
$R_{stab,CS}$ (T only)	**6.44**	5.02	2.91	1.55	2.18	1.39	0.94
Difference [%]	**-2.5**	-3.1	-3.5	-4.0	-8.8	-13	-16
$R_{stab,CS}$ (B only)	**6.48**	4.06	2.31	1.24	2.34	1.57	1.07
Difference [%]	**-2.0**	-22	-23	-23	-2.1	-1.6	-4.5
$R_{stab,CS}$(noT&B)	**6.31**	3.96	2.19	1.15	2.14	1.36	0.91
Difference [%]	**-4.5**	-24	-27	-28	-11	-14	-19
Buckled shape with truss and additional beam element							

Moment M_y	HEB300_tf19_tw11	HEB300_tf14.4_tw11	HEB300_tf12_tw11	HEB300_tf10.3_tw11	HEB300_tf14.4_tw3.5	HEB300_tf12_tw2.7	HEB300_tf10.3_tw2
$R_{stab,CS}$ (T&B)	**5.98**	4.01	3.18	2.67	2.57	1.77	1.28
$R_{stab,CS}$ (T only)	**5.80**	3.82	2.98	2.46	2.38	1.60	1.13
Difference [%]	**-3.0**	-4.9	-6.4	-7.8	-7.3	-10	-12
$R_{stab,CS}$ (B only)	**5.34**	3.49	2.70	2.19	2.44	1.68	1.05 (1.20)
Difference [%]	**-11**	-13	-15	-18	-5.0	-5.3	-18 (-6.25)
$R_{stab,CS}$(noT&B)	**5.19**	3.33	2.54	2.03	2.28	1.54	0.89 (1.01)
Difference [%]	**-13**	-17	-20	-24	-11	-13	-31 (-21)
Buckled shape with truss and additional beam element							

2.4. Comparison and conclusions

FINELg and CUFSM results have been compared for validation purposes. Fig. 12a plots an example of the observed differences between CUFSM and FINELg raw results. After the minimum eigenvalue is reached, results diverge between the two models; this is to be expected since CUFSM is based on the assumption that the buckling of each strip within the cross-section occurs in a sinusoidal half-wavelength that is equal to the length of the specimen while results obtained through shell F.E. models in FINELg have less restrictive constraints and may capture buckling with multiple half-waves in the longitudinal direction. This explains why FINELg results are roughly constant after the minimum eigenvalue is reached (see Fig. 12a). Hence, in Fig. 12b, and for sake of a consistent comparison between both sources, FINELg $R_{STAB,CS}$ values only associated with a buckling mode involving a single longitudinal half-wave have been kept. The graphical comparison displays an excellent accordance between both sources.
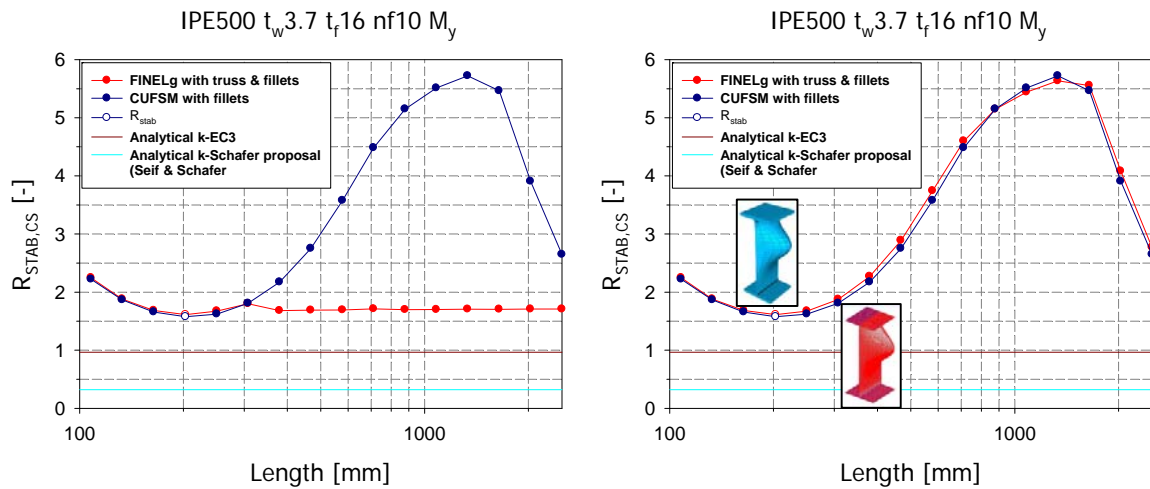

Figure 12: Example of a comparison between CUFSM and FINELg results

For all situations investigated, comparisons between CUFSM and FINELg results were performed and the minimum local buckling eigenvalue were compared. A deviation of maximum 12% was observed and the associated buckling shapes were identical. Based on these comparisons, which comprise different cross-section slenderness and two load cases (compression and major-axis bending), both software were shown to be suitable and have been used indifferently in the numerical calculation of $R_{STAB,CS}$.

3. Rotational capacity of wide-flange sections: F.E. parametric studies

3.1. Shell F.E. numerical models

Non-linear calculations were performed with the use of non-linear F.E.M. software FINELg (ULg and Greisch (2012)) with the objective of numerically predicting the rotational capacity. Further to the treatment of the web-to-flange zone, several modeling specificities were adopted to realistically simulate the mechanical behavior and offer a reasonable alternative to physical testing.

First, lateral torsional buckling has been prevented by fixing the transversal displacement of the flanges. This was intended at eliminating second order effects triggered by out-of-plane deflections which could influence the ultimate carrying capacity of the members. Too, stiffeners

11

were placed at the top flange load application section to enable a smooth load introduction and to avoid premature local web failure. For continuous beams (see Fig. 18, case 3), a stiffener was also placed at the middle support. The stiffener's thickness was set as the maximum thickness between the flanges and web. At the end supports, use of kinematic linear constraints and in-plane lateral support of the elements substituted the presence of stiffeners (see Fig. 13).
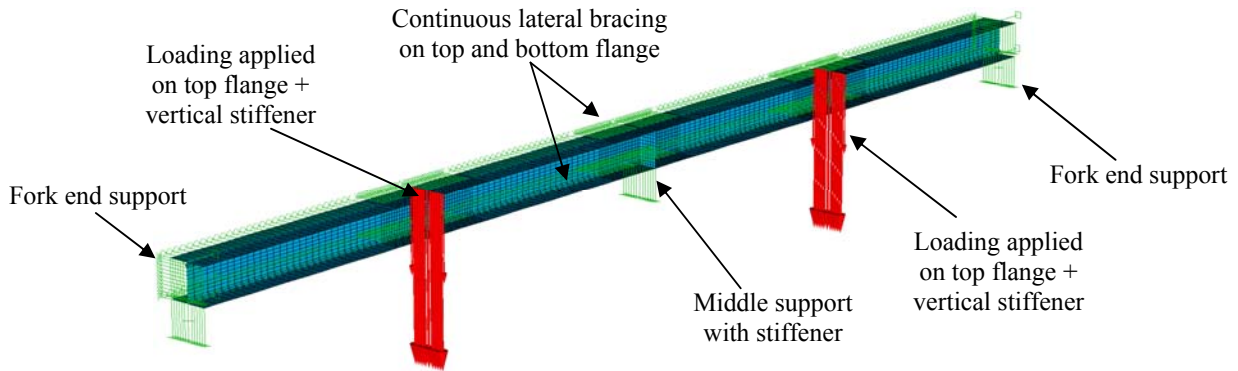
Figure 13: FINELg modelling details and load introduction (case 3)

The meshes adopted for web and flanges were similar to those defined in section 2. In the longitudinal direction, meshing was varied along the length (see Fig. 14). A refined mesh was used in zones where the development of plastic hinges is expected, i.e. in the vicinity of load application points and at the middle support for the continuous beams. The shell elements dimensions (length) were then gradually increased in zones with lesser influence on the structural behavior (Fig. 14b).
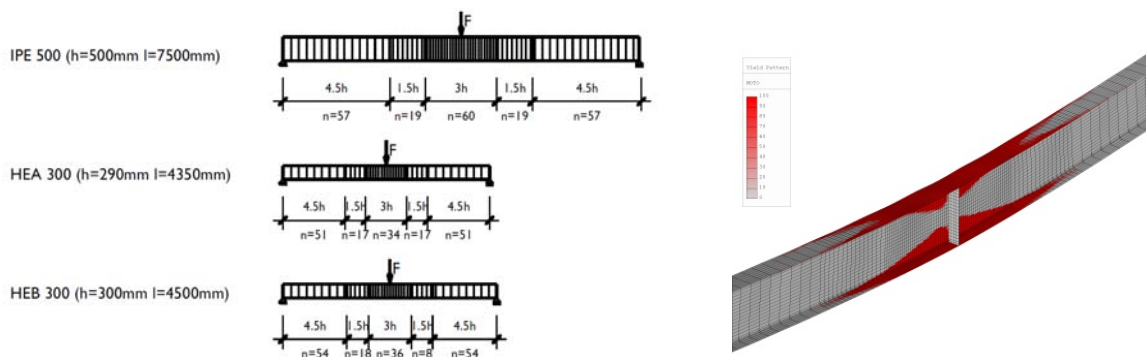
Figure 14: Example of mesh variation in the longitudinal direction

Typically, multi-linear material laws, such as those displayed in Fig. 15, were adopted, with key values as in Table 7. These correspond to state-of-the-art recommendations from E.C.C.S. (E.C.C.S. Publication N°44, 1986), and material standards (EN 10210). In the particular case of S690 steel grades (100 ksi steel), stricter limitations in terms of yield plateau length and level of ductility have been adopted.
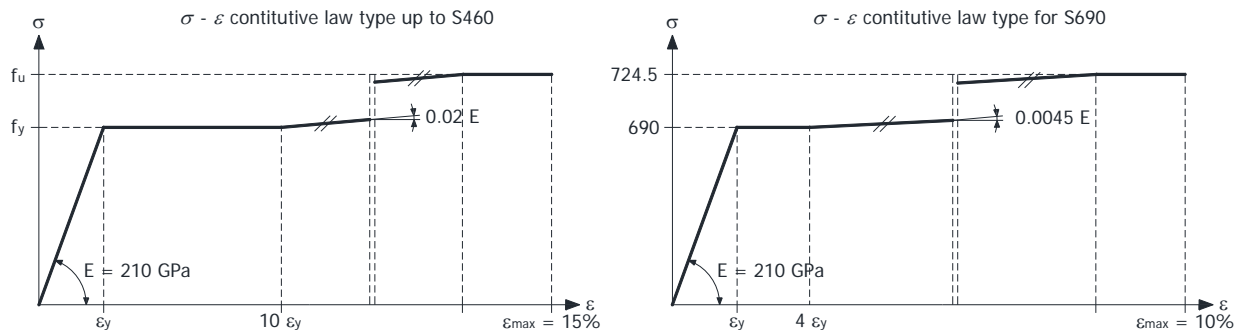
Figure 15: Adopted constitutive laws

Table 7: Adopted values for the steel constitutive laws

Steel Grade	f_y (N/mm^2)	f_u (N/mm^2)	ε_{max} (%)
S235 (36 ksi)	235	360	15
S460 (65 ksi)	460	550	15
S690 (100 ksi)	690	724.5	10

3.2. Imperfections

The definition of suitable initial imperfections is essential to the determination of both ultimate strength and post-buckling behavior of a member, and thereby deserves specific attention. First of all, material imperfections have been accounted for by means of parabolic auto-equilibrated residual stresses distributions. As for geometrical imperfections, only local imperfections were considered in the F.E. models since lateral torsional buckling was prevented.

A separate sensitivity analysis was conducted on two beams IPE500 (S235) and HEB300 (S460) with case 1 ($L / h = 3$) and case 2 ($L / h = 25$) static systems. The study considered the influence of different shapes and amplitudes of initial local geometric imperfections on the cross-section capacity of WF shapes. Basically, two ways of introducing initial imperfect shapes were considered. Type I considers imperfections introduced "manually" in the F.E. mesh through the definition of adequate (imperfect) node coordinates. Doing so allows for a free definition of the initial buckling waves, and also permits to set geometrical defaults in webs and flanges independently, both in shape and amplitude. More classically, type II resorts to linear buckling analysis in a preliminary step, whose first eigenmode shape is used to define the imperfect geometry of the girder, through the definition of adequate amplitudes.

In case of type I imperfections, the geometrical imperfect shape of each plate was built on the basis of sine, square half-waves in the longitudinal direction.
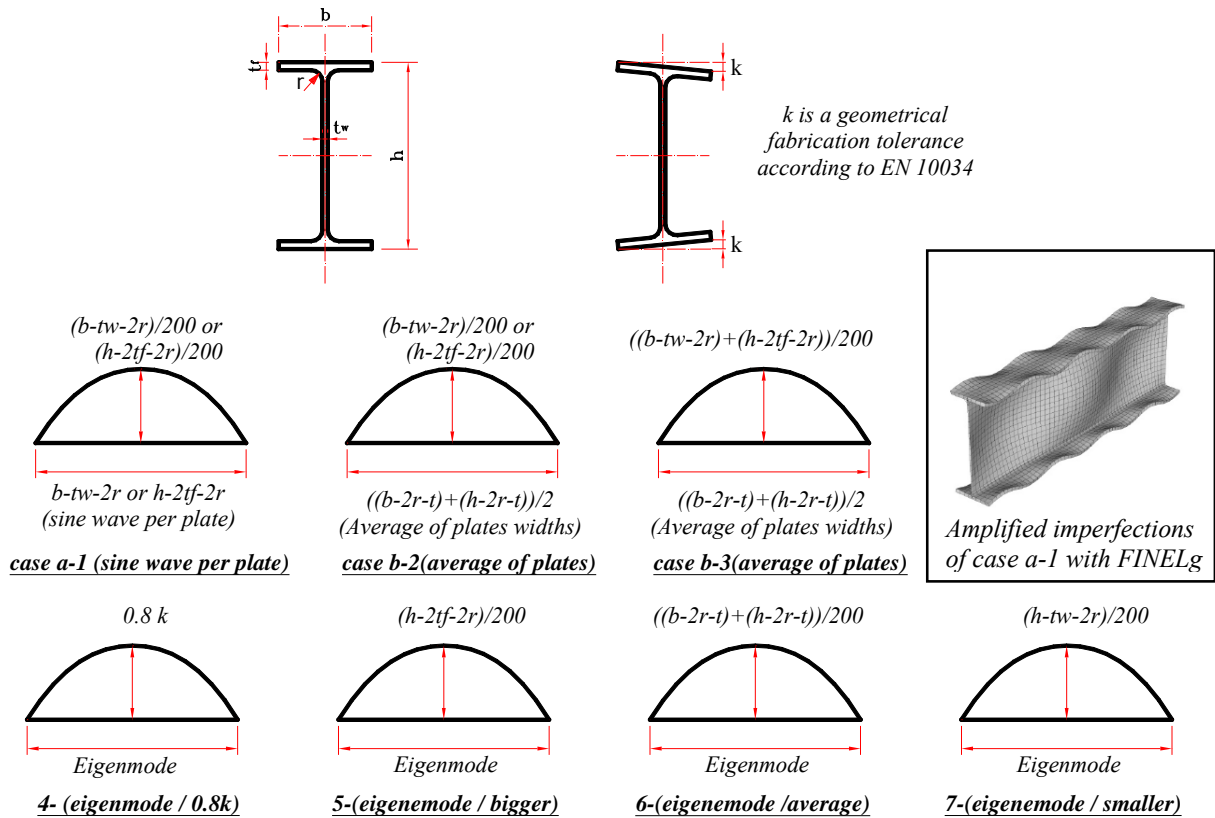
13

Figure 16: Adopted imperfections shapes and amplitudes

Type I-case a situations involved a fully independent definition of the half-wave periods between flanges and web (see Fig. 16). In the particular case of sections with a high h / b ratio (IPEs), this appears somehow inadequate. Case b definitions use equal wavelength in both flanges and web, defined as the average of the (flat) buckling lengths (i.e. $(h - 2r - 2t_f + b - 2r - t_w) / 2$). Different independent amplitudes in web and flanges may however be considered in the F.E. model.

As Fig. 16 shows, different amplitudes and shapes for the geometrical imperfections were tested and compared. It is observed on Fig. 17 that the non-dimensional ultimate moment M_{ult} / M_{pl} is slightly influenced by the different imperfections considered. However, they have a significant impact on the rotation capacity, especially for the IPE500 shape. Consequently, case b-3 imperfections with an averaged sine period and corresponding amplitude for each plate were selected. This choice was also motivated by the fact that initial imperfections are random and cannot realistically bear the shape of an eigenmode, together with the aim of remaining safe-sided.
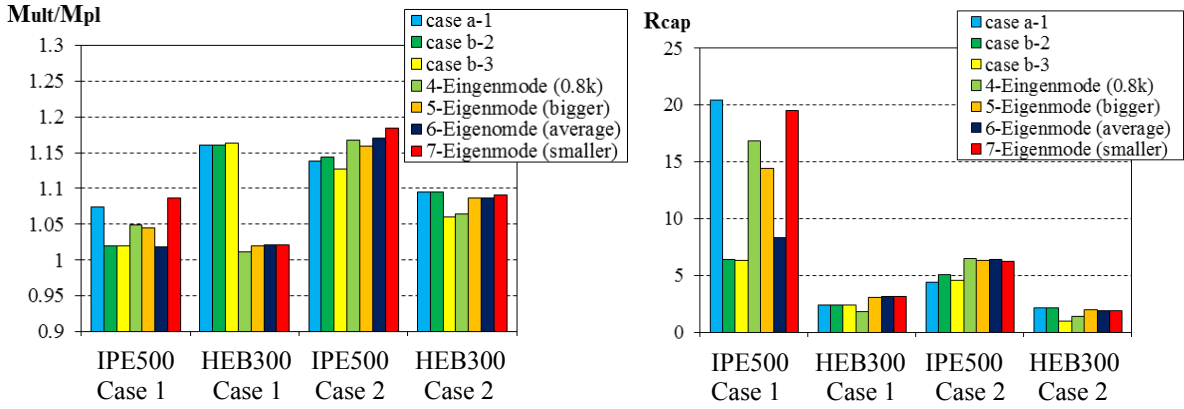
Figure 17: Influence of geometrical imperfections

3.3. Investigated parameters

Basically, three different bending configurations were considered: a simply supported beam under uniform moment (case 1), a simply supported beam under a concentrated force at mid-span (3-point bending configuration – case 2) and a two equal-span continuous beam with concentrated forces applied at each mid-span (case 3), see Fig. 18. The simply supported configurations aimed at characterizing the available rotation capacity, while the continuous beam arrangement aimed at characterizing the rotation demand and observing – or not – a plastic collapse mechanism. Profiles lengths were defined through the selection of a slenderness ratio L/h were L represents the length of a span and h the height of the section. For the case 1 configuration, the L/h ratio was chosen equal to three in order to i) define an initial local imperfection with three half-waves along the length of the beam and to ii) limit the influence of the edge support conditions. As for the case 2 and case 3 configurations, three different L/h were chosen (L/h = 15, 25, 35). These values were adopted so that the specimens are long enough for the beams to fail preliminary in bending and not in shear, and also to investigate different moment gradients. Three base profiles were chosen; IPE500, HEA300 and HEB300. Thicknesses of their webs and flanges were varied while their heights and widths were maintained constants in order to vary each plate's slenderness around the plastic-compact limit (class 1-2 limit). Three nominal yield stress f_y = 235, 460 and 690 N/mm^2 were considered.
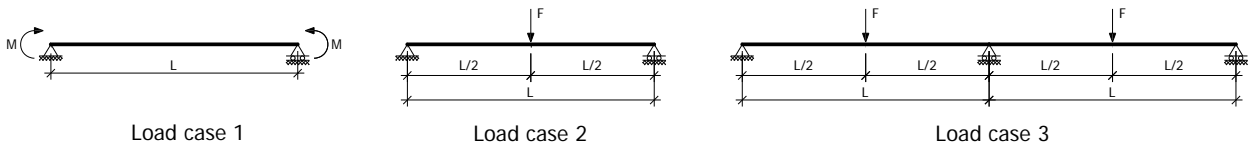

Figure 18: Description of static systems

4. Sensitivity analysis

As several definitions of the available rotation capacity R_{cap} can be found in literature, it is specified here that the present paper defines the available rotation capacity as reported in Eq. 2. In the finite element simulations, θ was calculated as the average rotation between the end sections rotations.

$$R_{cap} = \frac{\theta_u - \theta_{pl}}{\theta_{pl}}$$ (2)
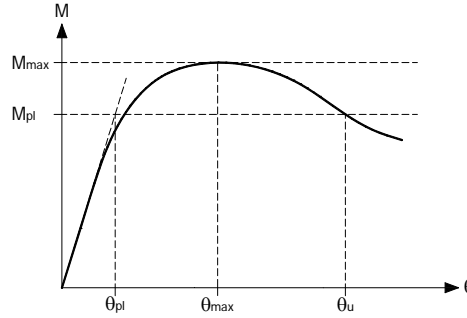

Figure 19: Graphical representation of R_{cap} definition

4.2. Benefits brought in considering section slenderness

As already explained, the intention is here to investigate whether or not the proposed $\lambda_{rel,CS}$ may be uniquely associated with a cross-section rotational capacity, i.e. a high level of ductility of the section in bending, such as is done in many standards through b/t limits. Figs. 19a and 19b allow this comparison, for the simply supported configurations.
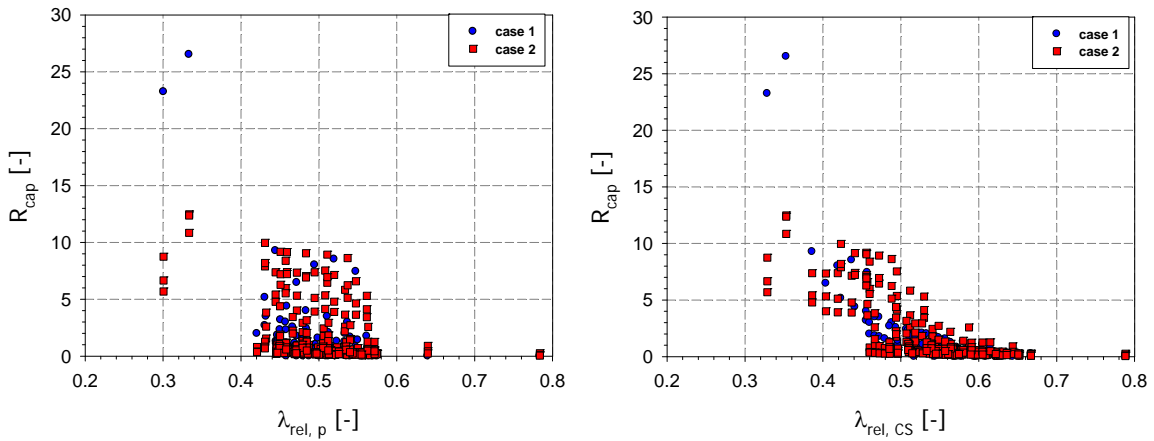
Figure 20: R_{cap} as a function of $\lambda_{rel,p}$ vs. $\lambda_{rel,CS}$

In Fig. 20, $\lambda_{rel,p}$ is taken as the maximum of $\lambda_{rel,p,flange}$ and $\lambda_{rel,p,web}$, where each $\lambda_{rel,p}$ value is relative to each plate assumed as being isolated from the others plates constituents (i.e. with "ideal" boundary conditions). On the contrary, $\lambda_{rel,cs}$ takes due account of these interactions, in considering the cross-section as a whole.

As can be observed, a more clear correlation between R_{cap} and $\lambda_{rel,cs}$ exists than between R_{cap} and $\lambda_{rel,p}$, where virtually no trend can be pointed out. A deeper look into Fig. 20b results can be achieved in separating results where one plate is clearly governing the cross-section behavior

from cases where interactions between the plates' constituents are expected. It is to be remembered here that unconventional cross-section dimensions have been defined in this purpose, see section 2.
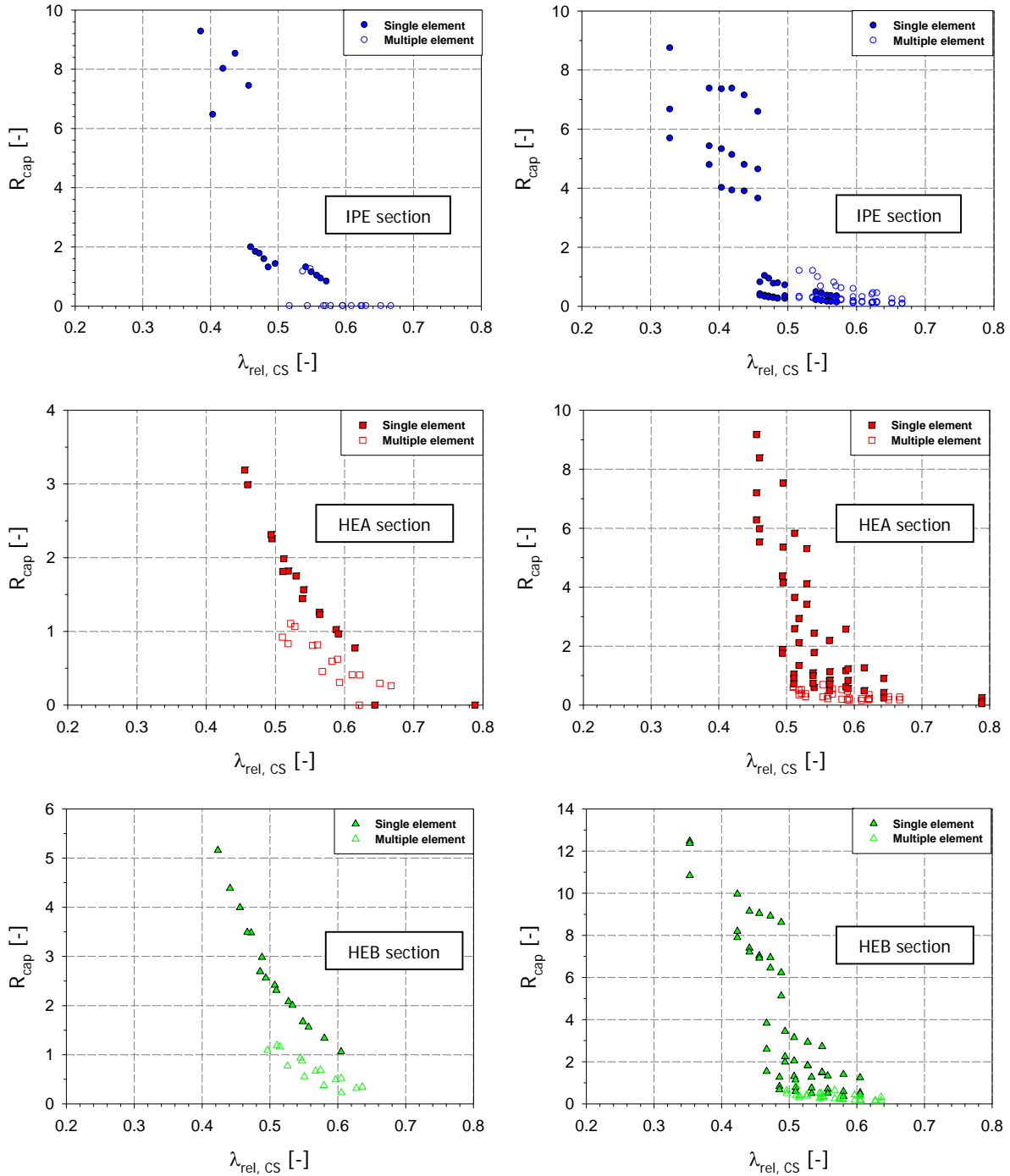
Single plate: one plate is governing the cross-section behavior
Multiple element: interactions between the plates' constituents are expected (multiple elements in coupled instabilities)

Figure 21: Influence of plates' interaction; load case 1 (left); case 2 (right)

Figs. 21a to 21f plot the obtained results for simply supported cases. For constant bending moment situations (case 1, left graphs in Fig. 21), the detrimental influence of plates' interactions is obvious, whatever the cross-section shape. For case 2 situations (3-point bending), identical observations shall be made, although the influence of shear and moment gradient on R_{cap} causes the interpretation of results more delicate – cf. § 4.3. Accordingly, a complementary factor ξ_p has been defined as follows:

$$\xi_p = \frac{\max\left(\lambda_{rel,p,flange}; \lambda_{rel,p,web}\right)}{\min\left(\lambda_{rel,p,flange}; \lambda_{rel,p,web}\right)} \tag{3}$$

ξ_p is aimed at characterizing the theoretical expected level of interaction between plates. Low ξ_p values indicate strong interactions (i.e. the first plate to be affected by local buckling shall not receive an important "support" for the adjacent ones, themselves being concerned with their own instabilities soon after); in contrary, high ξ_p values relate to situations where the stability behavior of the cross-section is mostly governed by one single element.

Figs. 22a and 22b allow partially validating the use of ξ_p as a second key parameter associated with R_{cap}, in addition to $\lambda_{rel,CS}$. As Fig. 22b shows, a $\xi_p = 1.2$ limit value may be adopted to characterize cases strongly affected by plates interactions – all $\xi_p \leq 1.2$ cases show limited R_{cap} values, i.e. $R_{cap} \leq 1$. Fig. 22b also suggest, for case 2 situations, that additional influences such as primary shear or moment gradient play a significant role, as already pointed out by Kulhmann (Kulhmann 1989), since results with $R_{cap} \leq 1$ are observed for $\xi_p \leq 1.2$ values in these cases.
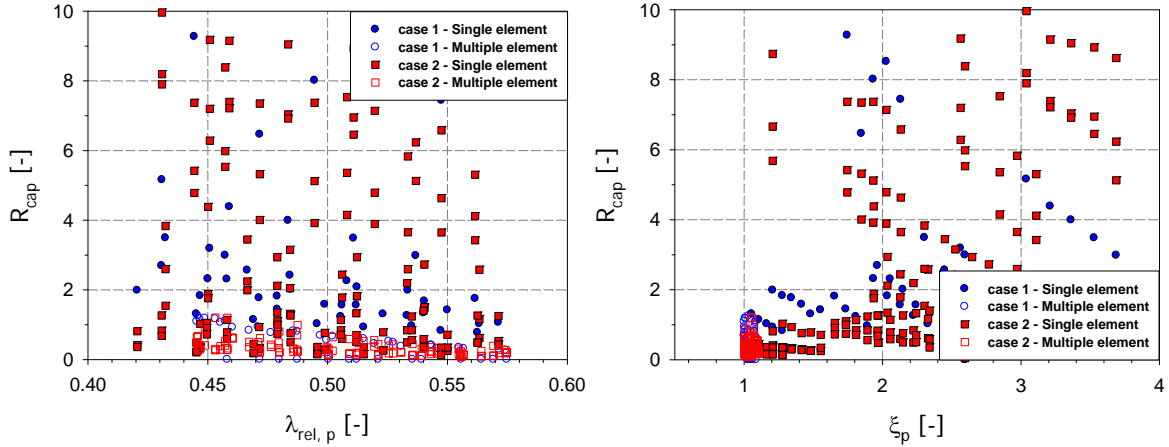
Figure 22: Influence of ξ_p and the plate slenderness $\lambda_{rel,p}$ on the available rotational capacity R_{cap}

As an alternative, flange-to-web stiffness ratios have also been considered, as reported on Figs. 23a and 23b, where $L_f = b - 2r - t_w$ and $L_w = h - 2r - 2t_f$.
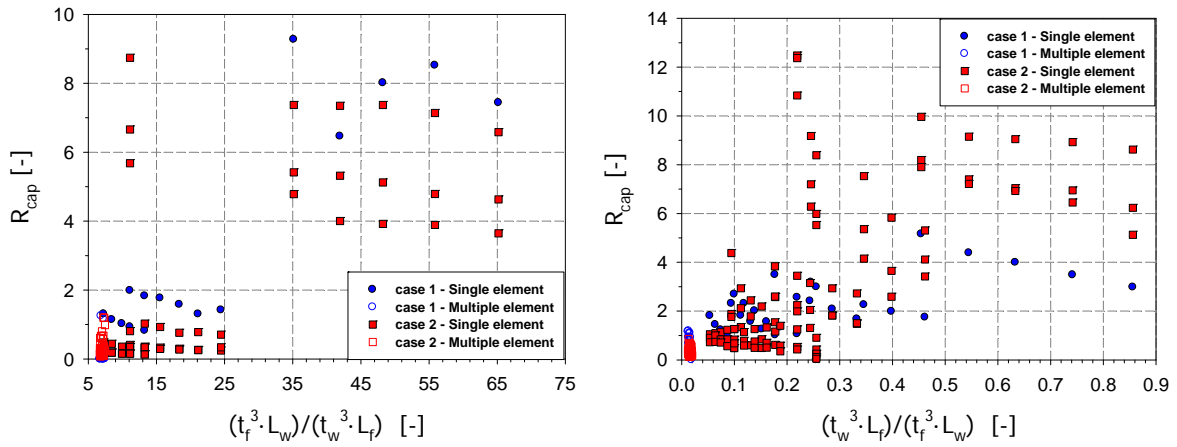
Figure 23: Influence of the plate stiffness ratios on the available rotational capacity R_{cap}; a) IPEs – b) HE sections

Considering the relatively bad correlation and since this last attempt do not take due account for the cross-section overall dimensions and shape (IPEs governed by web buckling or HE sections governed by web buckling) nor the steel grades, the $\xi_p \leq 1.2$ criterion has been kept further to characterize situations with strong plate interactions. Figs. 24a to 24f propose the obtained results for the present numerical database (cases 1 and 2).
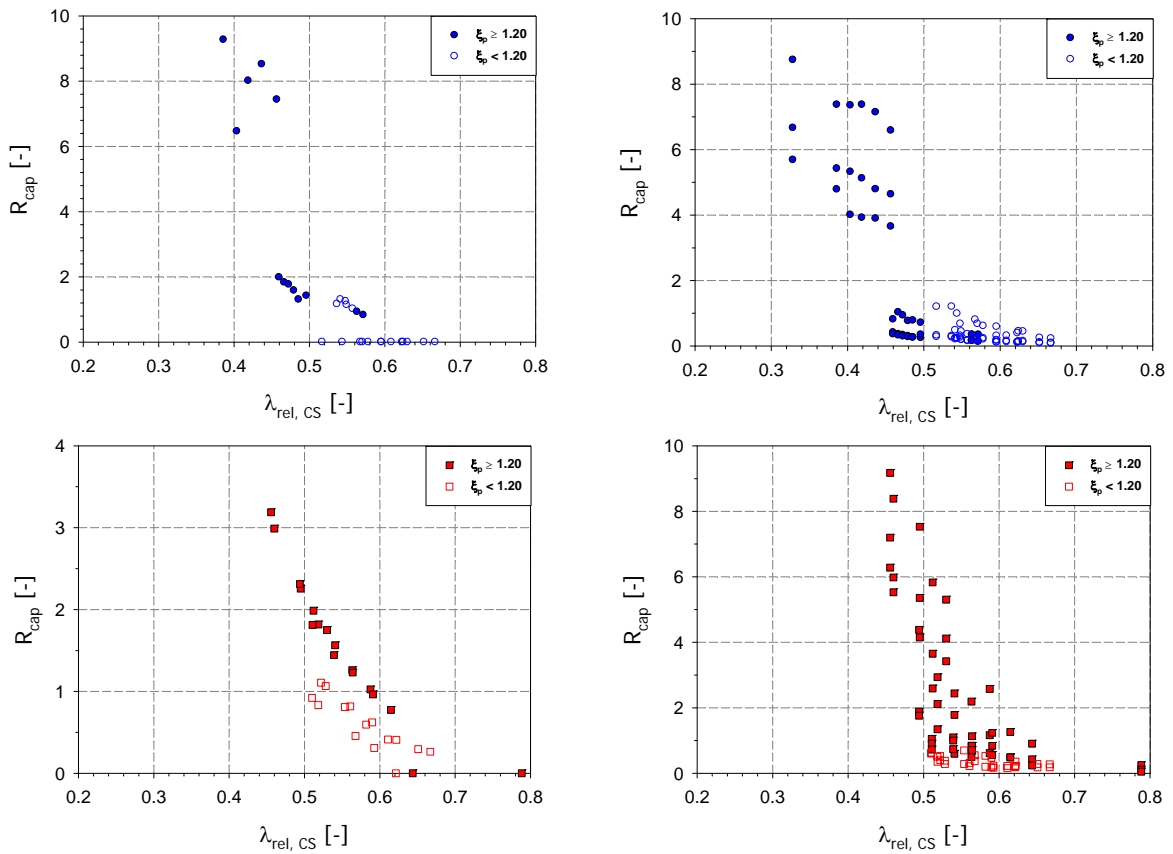
Figure 24: Influence of ξ_p on the available rotational capacity R_{cap}; IPE sections (left) – HE sections (right)

Thus, although being strictly defined on the basis of resistance/stability parameters, ξ_p is seen to somehow reflect the capacity of a cross-section to reach high $R_{ca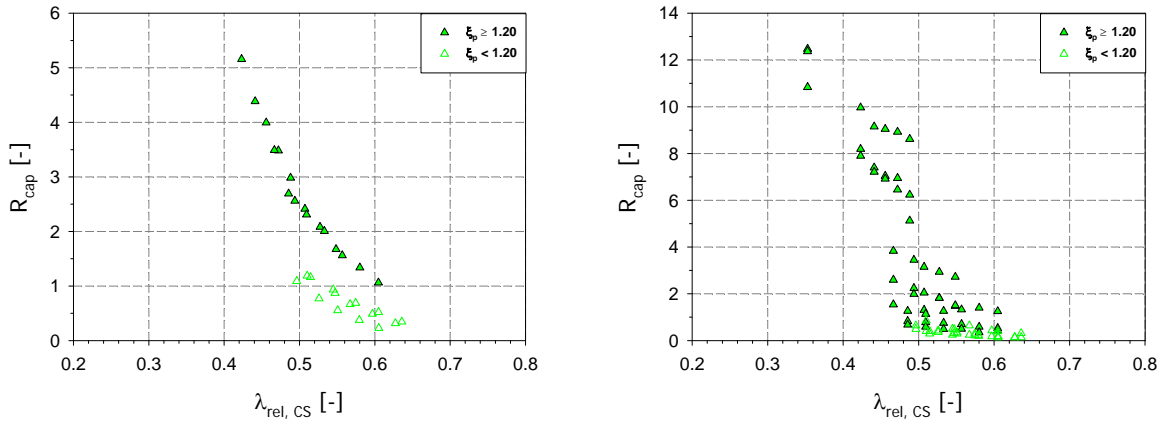p}$ values. The following particular example (see also Fig. 24) precisely illustrates this; case A is associated with a weak flange compared to the web ($\xi_p = 3.69$), while case B has equally weak flanges and web through modified thicknesses ($\xi_p = 1.00$).

The associated M-θ curves and R_{cap} values, for a nearly identical $\lambda_{rel,CS} \approx 0.5$ value show that the use of ξ_p may nicely complement $\lambda_{rel,CS}$ to predict the rotation capacity. It may also be interesting to note that, owing to material ductility and despite the "cross-section effect" that drastically penalizes the overall level of cross-sectional deformation capacity, case A top flange early buckling does not precludes the attainment of high strains, so as the cross-section to exhibit a relatively high $R_{cap} = 2.98$ value; on the contrary, case B leads to a $R_{cap} = 1.09$ value.

Deformed shape of HEB300 case A

HEB300 S235; case 1: $L = 3\,h$		
	Case A	Case B
t_f (mm) =	11.8	14.7
t_w (mm) =	11.0	3.50
$\lambda_{rel,p,flange}$ (-) =	0.537	0.445
$\lambda_{rel,p,web}$ (-) =	0.146	0.445
$\lambda_{rel,CS}$ (-) =	0.49	0.50
ξ_p (-) =	3.69	1.00
R_{cap} (-) =	2.98	1.09
M_{max}/M_{pl} (-) =	1.013	1.015
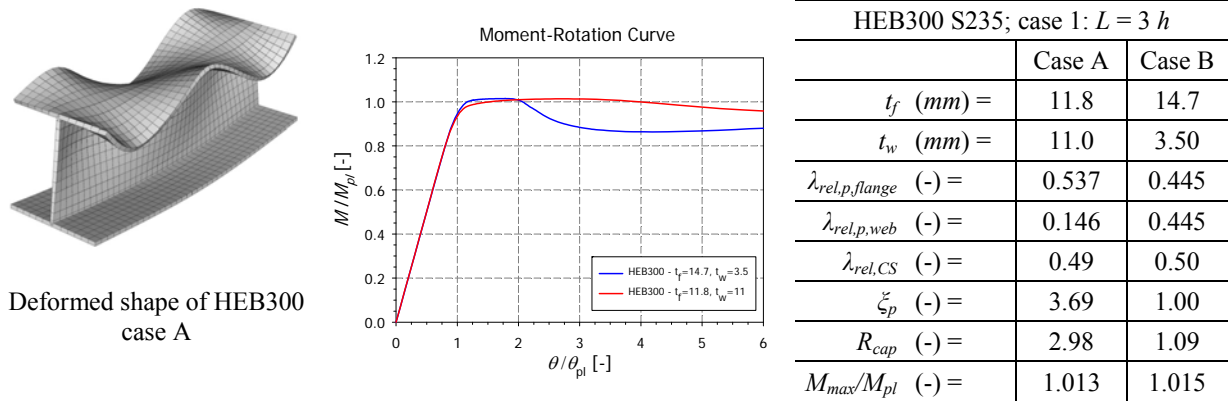
Figure 25: Moment - rotation response of two "HEB300-based" sections

This observation is in contradiction with the usual treatment of R_{cap} in design codes such as Eurocode 3, since R_{cap} is only associated with a single $\lambda_{rel,p}$ value. Accordingly, identical $\lambda_{rel,p}$ shall lead to identical R_{cap} values, which, as Fig. 24 shows, may be suitable for case 1 situations (left plots) but not for case 2 situations (right plots). As an example, Fig. 25b provides, for a given $\lambda_{rel,CS} \approx 0.5$, R_{cap} values from 0 to 8. Hence, the approach is seen to be inappropriate and the need for additional parameters to be included or new criteria to be developed are evidenced by these results.

4.3. Influence of shear

Since a high level of shear force is known to have an important (detrimental) influence on the resistance to bending (Eurocode 3 (CEN 2005), US standards (AISC 2005)), present paragraph is devoted to the influence of shear on the rotation capacity. In Eurocode 3, W.F. sections are implicitly assumed as resisting shear through their webs, while the flanges mostly carry bending moments; a reduction in (plastic) bending capacity is only necessary when the applied shear force V exceeds 50% of V_{pl}, where V_{pl} designates the plastic shear capacity:

$$V_{pl} = A_v \frac{f_y}{\sqrt{3}} \tag{4}$$

A_v being constituted by the webs, fillets and a small part of the flanges in the vicinity of the web-flange junction. Because bending resistance and cross-sectional rotational capacity shall be associated to different mechanical natures (resistance vs. ductility), the question whether shear bears the same influence on R_{cap} remains open. As Fig. 26 shows, a correlation between R_{cap} and the V / V_{pl} ratio is not obvious on IPE sections, where high R_{cap} values (i.e. $R_{cap} \geq 3$) as well as low ones may be reached for varying V / V_{pl} ratios; results for HEA and HEB sections are however more distinct (see Fig. 25a), where a high level of shear force is systematically associated with low R_{cap} values; this observation shall however be tempered by the fact that many of these results are related to sections characterized by low ξ_p ratios. Accordingly, no direct and obvious influence of the level of shear force on the cross-section rotational capacity shall be drawn at this point.
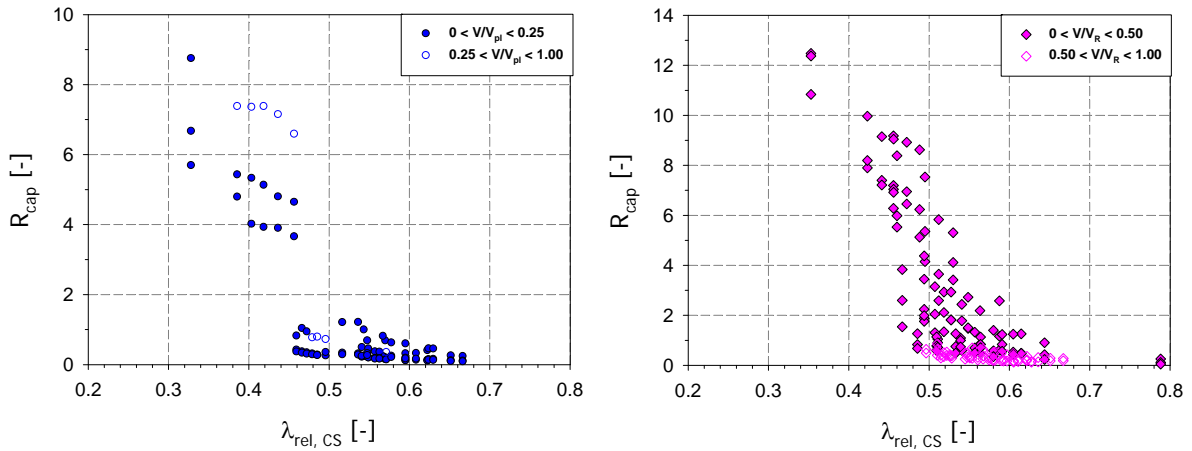
Figure 26: Influence of shear ratio on the rotation capacity R_{cap}; a) IPE sections – b) HE sections

4.4. Influence of steel grade

The use of different steel grades, with a higher relative influence of local buckling, different maximum strain values ε_{max} and f_u / f_y ratios, shall affect cross-section rotational capacity as well. In general, HEA and HEB sections were observed to lead to a decrease in rotation capacity when the steel grade increased. However, this trend was less clear for the IPE sections as they are seen to possess a smaller rotation capacity compared to the HE sections, cf. Figs. 27a to 27d.

Figure 27: Influence of steel grade on R_{cap}

4.5. Influence of L / h ratio

Present paragraph only refers to load case 2 situations. When the L / h ratio varies, the moment gradient also varies and affects the rotational capacity. Indeed, local buckling only develops once the compression flange has yielded over 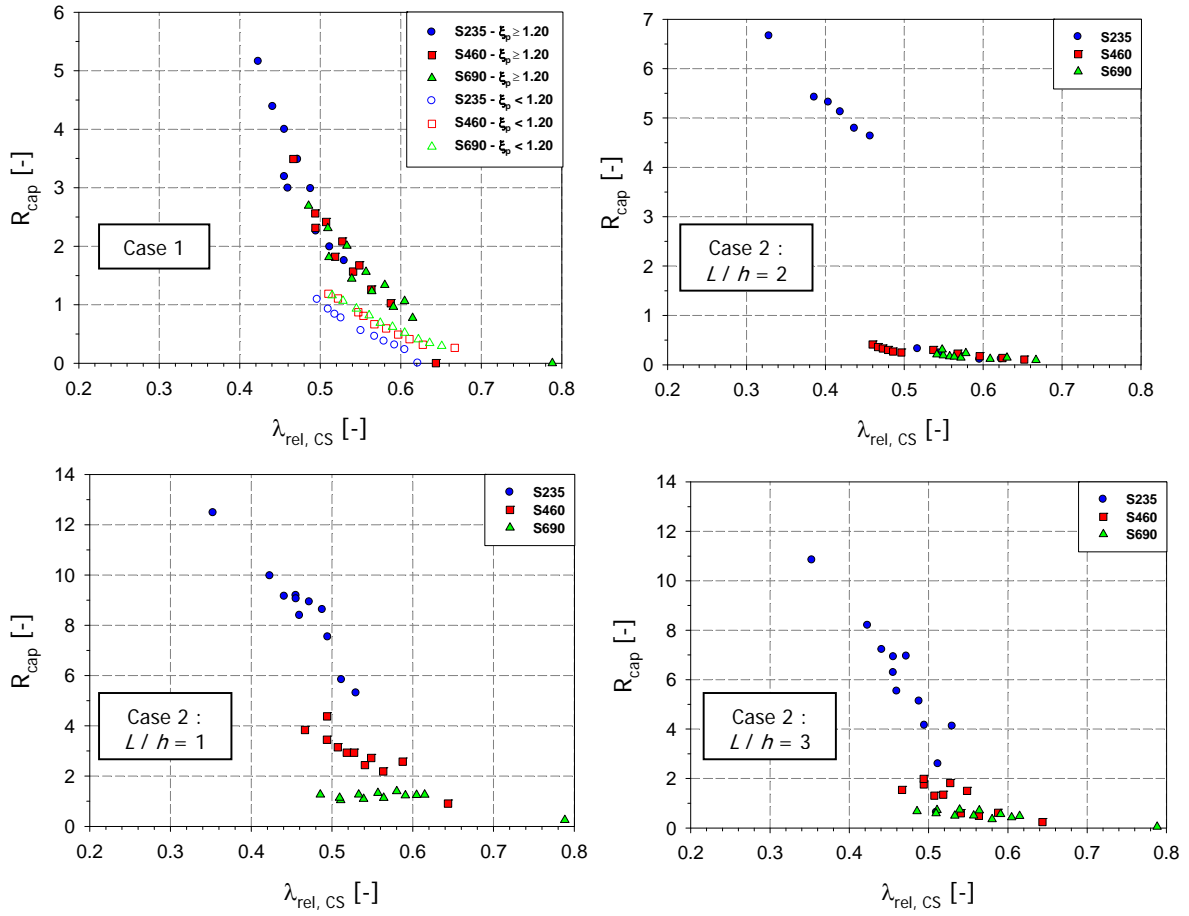a sufficient length so that a buckled shape roughly equal to 120% of the width of the flange in compression is able to develop. Hence, with a steep moment gradient, yielding of the beam is confined to the adjacent region of maximum moment and will start to extend longitudinally when the plastic moment M_p is reached. Therefore, when the L / h ration increases, the steepness of the moment gradient decreases and lower rotation capacities values are attained. Fig. 28a and 28b show examples of results displaying different L / h ratios; they refer to case 2 situations (3-point bending) for which the influence of shear can be disregarded ($V / V_{pl} \leq 0.5$) – case 1 results are also plotted for comparison purposes –. From these figures, it is clear that the rotation capacity increases when the L / h ratio increases, i.e. the slope of the moment gradient in the plastic hinge zone is more pronounced. This obviously has to be associated with a more favorable extent of yielding along the longitudinal axis of the beam, since, for shorter beams, the moment gradient is steeper so that the elastic regions in the vicinity of the plastic hinge tend to more easily mobilized. Similar observations were made for all steel grades, in an even clearer extent for IPE-based sections for which the webs usually controls the mechanical behavior.
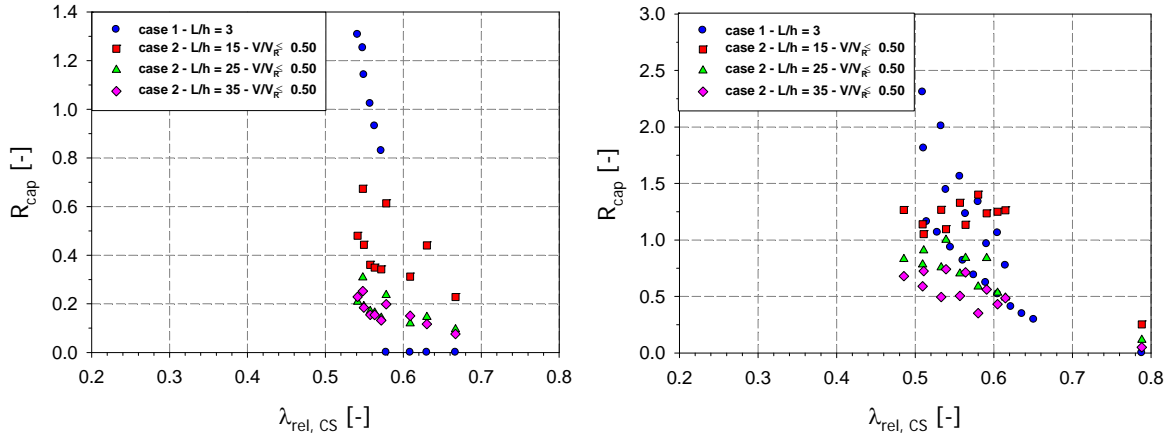
Figure 28: Influence of *L / h* for S690; a) IPE sections − b) HE sections

Figs. 29a and 29b also report the results for case 1 situations where a constant bending moment is applied. For the HE cases, rotation capacities were lower than their non-zero moment gradient counterparts. In contrast, for the IPE sections, results were contradictory, leading to both higher and lower rotation capacities for case 1 configurations.
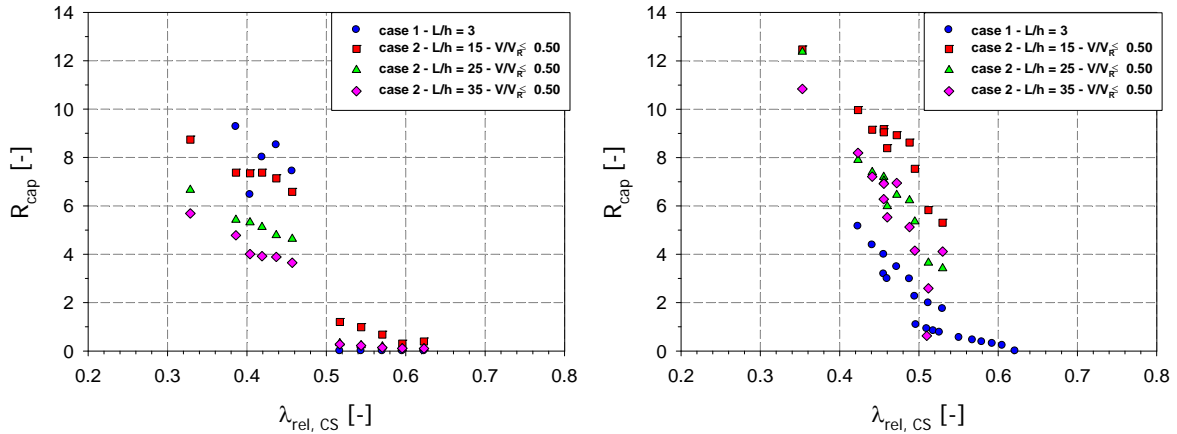

Figure 29: Influence of *L / h* for S235; a) IPE sections − b) HE sections

4.6. Rotational capacity: demand vs. availability

Having exposed aspects related to the available rotation capacity, present paragraph is dedicated to the characterization of the demand versus available rotation capacity, through case 3 finite element results. The latter shall constitute a database of numerical reference results allowing separating cases where a full plastic mechanism could be reached (development of three plastic hinges, i.e. $R_{dem} < R_{cap}$ and plastic analysis is allowed) from those who could not (system collapse load is lower than theoretically predicted one, $R_{dem} > R_{cap}$ and plastic analysis should be prevented). In this respect, Figs. 32a and 32b indicate and separate cases who could not reach at least 98% of the theoretical system plastic limit load – relatively few cases are to be reported.

Focusing on results for which a full collapse mechanism could be reached, the possibility to discuss alternative criteria to Fig. 1 one becomes open. In particular, one may refer to the following ones:
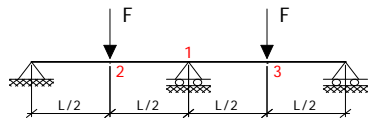
23

$$R_{cap} \geq 3.0 \qquad (5)$$

$$\lambda_{rel,p} \geq 0.5 \qquad (6)$$

Both Eq. 5 and 6 criteria represent an indirect alternative to Fig. 1 one ($R_{dem} < R_{cap}$); one may also report the class 1-2 limits in Eurocode 3 classification system as another well-known one, but the background of these limits lies in the adoption of b / t limits based on Eq. 6, so that the latter was not considered further. These criteria however only rely on prescribing a minimum level of available rotation capacity to authorize a plastic analysis, regardless of the rotation demand.

In the particular case 3 configuration considered here, it is relatively easy to reach the theoretical $R_{dem} = 0.25$ value from Table 8 data as follows:

$$R_{dem} = \frac{\theta_{pl2,3} - \theta_{pl1}}{\theta_{pl1}} = \frac{\theta_{pl2,3}}{\theta_{pl1}} - 1 = \frac{5FL^2 / 128EI_y}{FL^2 / 32EI_y} - 1 = 0.25 \qquad (7)$$

Table 8: Theoretical limit values

(beam diagram with F loads, sections 2, 1, 3, spans L/2, L/2, L/2, L/2)	$F_{pl,z1} = 16 \cdot M_{pl,y} / (3L)$	$\theta_{pl1} = \frac{M_{pl,y}}{EI} \cdot \frac{L^2}{32}$
	$F_{pl,z2} = F_{pl,z3} = \frac{9}{8} \cdot F_{pl,z1}$	$\theta_{pl2,3} = \theta_{pl1} + \frac{F_{pl,z2} / 8}{EI} \cdot \frac{L^2}{16}$

Owing to symmetric loading and equal spans, the first plastic hinge forms at the middle support (section 1), for a $F_{pl,z1}$ load level; additional bending moments are then redistributed to the sagging regions until simultaneous development of hinges at sections 2 and 3 is effective, and a plastic collapse mechanism formed. The corresponding system collapse load and θ_{pl} are calculated through virtual work principles and an assumed elastic distribution of bending moments in the rigid beam segments between plastic hinges.

The $R_{dem} = 0.25$ value, based on the well-known "plastic hinge theory", is to be discussed when predicted through the finite element shell models. Indeed, the assumption of a zero-length plastic hinge is obviously not reflected numerically. Also, the numerical models made use of more sophisticated material laws (see Fig. 15) than the theoretically-assumed rigid-plastic one; in particular, strain hardening effect may deeply affect the system response, especially for low steel grades.

Figure 30: Typical plastic failure mode for case 3 configuration (yield pattern, HEB section)

All these aspects are reflected in Fig. 31a, regrouping all numerical results that were observed to develop a plastic mechanism. The figure shows that the rotational demand slightly varies around the 0.25 theoretical value, with respect to various influences. First of all, situations where local buckling of one single element governs the behavior ($1.10 < \xi_p < 4.00$) are seen to reach R_{dem} values slightly lower than 0.25. In contrast, situations where cross-section plates may exhibit an interactive local buckling ($\xi_p < 1.10$) display more variable responses, with R_{dem} values ranging from 0.20 to 0.45. This variability is also observed for the HE sections (Fig. 31b), and, further to a dependency to ξ_p and steel grade, can be shown to be associated with the influence of the moment gradient through the L / h ratio – Fig. 31b also plots results for which the influence of shear can be eliminated (i.e. $V / V_R < 0.50$).
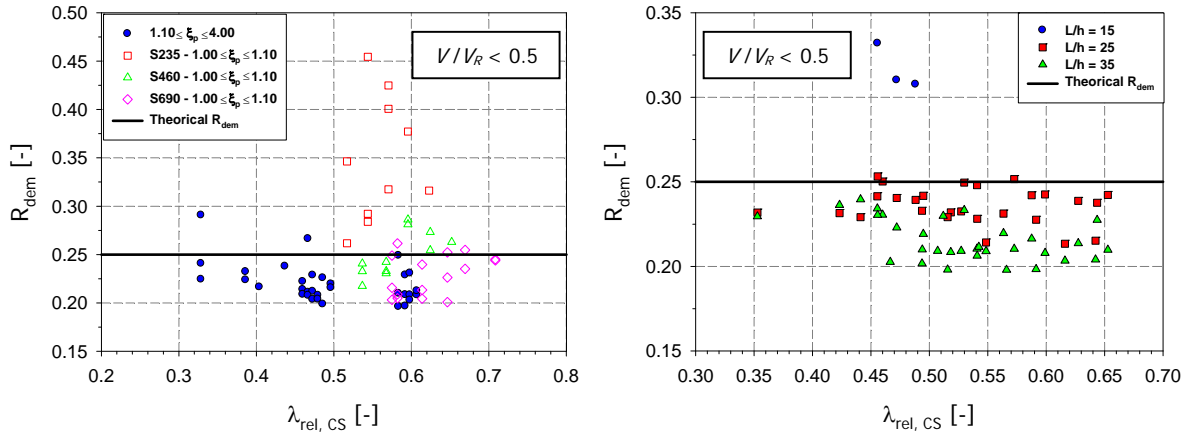

Figure 31: Comparison of theoretical and FINELg predictions in terms of rotational demand; a) IPE sections, b) HE sections

Figs. 32a and 32b propose another representation of all case 3 results, with respect to $\lambda_{rel,p}$ and $\lambda_{rel,CS}$, respectively. They allow checking the relative pertinence of Eqs. 5 and 6 with respect to the $R_{dem} < R_{cap}$ criterion. Their analysis yields the following observations and conclusions:

- A relatively low number of cases could not reach the plastic collapse mechanism;

- Eq. 5 criteria, here leading to $R_{dem} / R_{cap} = 0.083$ and represented through the blue vertical lines in Fig. 32, is clearly seen to be inappropriate, in allowing too few situations to resort to plastic analysis than what the numerical analyses show. These too restrictive predictions were obviously expected, given the low R_{dem} values around 0.25;

- Eq. 6 proposal appears to be inappropriate as well, however in a lesser extent as seen in Fig. 32a. Indeed, it both yields "false" predictions (cases where $\lambda_{rel,p} < 0.5$ but $R_{dem} / R_{cap} > 1.0$ results) and too conservative results (cases with $\lambda_{rel,p} > 0.5$ but plastic analysis to be allowed, $R_{dem} / R_{cap} < 1.0$). Fig. 32b also shows that $\lambda_{rel,CS} < 0.5$ could be a safer alternative, as no results with a $\lambda_{rel,CS} < 0$ but $R_{dem} / R_{cap} > 1.0$ are observed; nevertheless, this alternative shall be seen as too restrictive as well, many results with $\lambda_{rel,CS} > 0.5$ but $R_{dem} / R_{cap} < 1.0$ being reported here. Therefore, additional research is needed to deal with these last results through a $\lambda_{rel,CS}$-based criteria that shall obviously incorporate all key parameters influences detailed in the previous paragraphs.
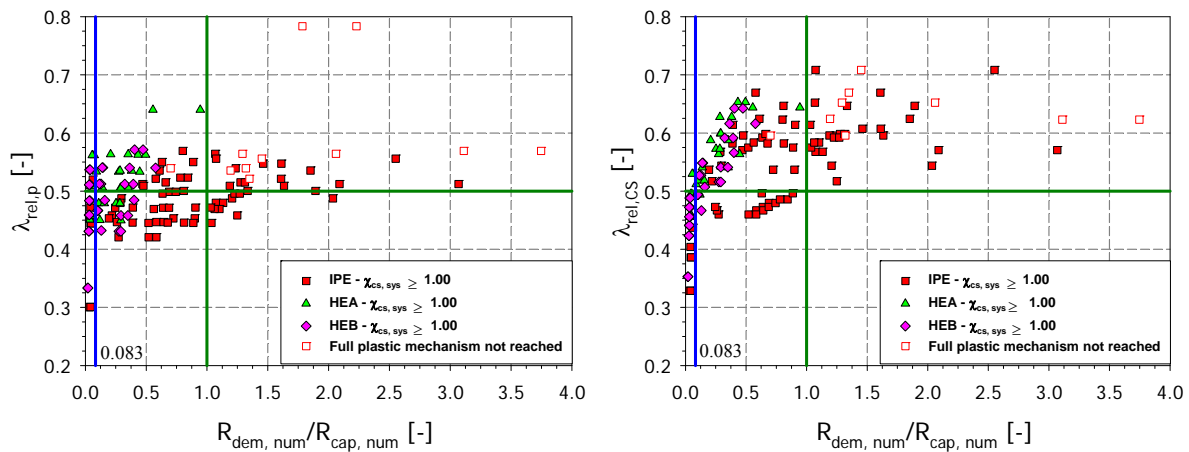
Figure 32: Various criteria to allow plastic analysis

5. Conclusions and future steps

The present paper, dedicated to the study of wide flange sections rotational capacity, was aimed at investigating in which extent an original overall cross-section relative slenderness $\lambda_{rel,CS}$ could be used in separating sections allowing plastic collapse mechanism from these who cannot.

In a first step, the paper discussed a key parameter $R_{STAB,CS}$ in the calculation of $\lambda_{rel,CS}$. It showed that the use of either finite strip method-based tool (CUFSM in the present case) or shell finite element software could be equally used for a numerically prediction of $R_{STAB,CS}$, provided special attention is paid to the web-to-flange area modelling.

Then, the paper described shell finite element parametric studies led to characterize both the rotational capacity and the rotational demand, with respect to many parameters such as shear, steel grade, moment gradient, cross-section geometry, … Particular attention was devoted to discussing the shapes and amplitudes of geometrical initial imperfections, which were shown to be a highly influential parameter on R_{cap} values.

Last, section 4 investigated the relative influence of key parameters on the rotational capacity, and discussed the potentiality to use a $\lambda_{rel,CS}$-based criterion to allow for a plastic analysis. On the basis of the considered configuration, it was found that although providing more consistent results than the traditional use of $\lambda_{rel,p}$, the sole use of $\lambda_{rel,CS}$ could not lead to satisfactory predictions. Additional developments are needed to provide a better selection of situations where plastic design could be allowed, in associating $\lambda_{rel,CS}$ with other key parameters as studied herein.

References

Arcelor Mittal, Tableau 14 - Tolérances de laminage poutrelles,» *[Online] : http://ds.arcelormittal.com/repo/ poutrelles_rails_tubes_parachevement_negoce/tolerances_laminage_poutrelles.pdf.*

Boissonnade N., Somja H. (2012). "Influence of Imperfections in F.E.M. Modeling of Lateral Torsional Buckling." *Proceedings of the Annual Stability Conference, Structural Stability Research Council.*

Boissonnade N., Nseir J. Saloumi E. (2013). "The Overall Interaction Concept: an Alternative Approach to the Stability and Resistance of Steel Sections and Members." *Proceedings of the Annual Stability Conference, Structural Stability Research Council, St. Louis, Missouri, April 16-20.*

Bild S., Kulak G. (1991). "Local Buckling Rules for Structural Steel Members." *Journal of Constructional Steel Research vol. 20, pp. 1-5.*

CEN (Comité Européen de Normalisation) (2005). "Eurocode 3: Design of Steel Structures, Part 1–1: General rules and rules for buildings (EN 1993-1-1)", Brussels.

CEN (Comité Européen de Normalisation) (2005). "Eurocode 3: Design of Steel Structures, Part 1–5: Design of plated structures (EN 1993-1-1)", Brussels.

CEN (Comité Européen de Normalisation) (2007), Eurocode 1993-1-12 Calcul des structures en acier "Règles additionnelles pour l'utilisation de l'EN 1993 jusqu'à la nuance d'acier S 700".

Chen Y., Cheng X. , Nethercot D. (2013). "An overview study on cross-section classification of steel H-sections." *Journal of Constructional Steel Research vol. 80, pp. 386-393.*

ECCS Publication N°44 (1986). "Behaviour and Design of Steel Plated structures."

EN 10210-2: "Hot finished structural hollow sections of non-alloy steels."

Gerard G. , Becker H. (1957). "Technical note 3781 - Handbook of Structural Stability - Part. 1 - Buckling of Flat Plates." *National Advisory Committee for Aeronautics*, Washington: NACA.

Gardner L., Saari N. et Wang F. (2010). "Comparative experimental study of hot-rolled and cold-formed rectangular hollow sections." *Journal of Constructional Steel Research* vol. 48, pp. 495-507.

Gioncu V. , Anastasiadis A. (2013). "Plastic coupled instabilities of I-shaped steel beams" *Thin-Walled Structures,* p. 11.

Gioncu V., Petcu D. (1997). "Available Rotation Capacity of Wide-Flange Beams and Beam-Columns - Part 2 - Experimental and Numerical Tests." *Journal of Constructional Steel Research vol. 43, pp. 219-245.*

University of Liège ULg and Greisch Engineering Office (2012). non-linear F.E.M. software FINELg.

Hirt M., Nussbaumer A., Crisinel M., Lebet J. (2004). Complément au Traité de Génie Civil - Construction métallique "Bases de calcul et exemples numériques adaptés aux nouvelles normes", *PPUR presses polytechnique.*

Hirt M., Bez R., Nussbaumer A. (2011). "Notions fondamentales et méthodes de dimensionnement." *PPUR presses polytechniques, Traité de Génie Civil vol. 10 - Construction métallique*

Johansson B., Maquoi R., Sedlacek G., Müller C., Beg D. (2007). "commentary and worked examples to EN 1993-1-5 plated structural elements." *JRC (Joint research committee),* Joint Report, First Edition, EUR 22898, EN - 2007

Kato B. (1989). "Rotation Capacity of H-Section Members as Determined by Local Buckling" *Journal of Constructional Steel Research* vol. 13, pp. 95-109.

Kato B. (1990). "Deformation Capacity of Steel Structures." *Journal of Constructional Steel Research* vol. 17, pp. 33-94.

Li Y. (2013), "Extension of the Direct Strength Method to hot-rolled and welded cross-sections." *PhD presentation - Université de Liège.*

Kettler M. (2008). "Elastic-plastic cross-sectional resistance of semi-compact H- and hollow sections." *PhD Thesis - Graz Technical University.*

Kuhlmann U. (1989). "Definition of Flange Slenderness Limits on the Basis of Rotation Capacity Values." *Journal of Constructional Steel Research* vol. 14, pp. 21-40.

Shokouhian M., Shi Y. (2014). "Classification of I-section flexural members based on members ductility". *Journal of Constructional Steel Research* vol. 95, pp. 198-210.

Schafer B. , Seif M. (2007). "Cross-section Stability of Structural Steel." *AISC Faculty Fellowship*, Progress Report No. 1, p. 74.

Schafer B. (2013). "Thin-Walled Structures, Ben Schafer, JHU, Cold-Formed Steel, CUFSM, Elastic Buckling, Direct Strength Method." *[On line]. Available: http://www.ce.jhu.edu/bschafer/index.htm.*

Seif M., Schafer B. (2010). "Local buckling of structural steel shapes." *Journal of Constructional Steel Research* vol. 66, pp. 1232-1247.

Boeraeve Ph., Lognard B., Janss J., Gérardy J.C., Schleich J.B. (1993). "Elasto-plastic Behaviour of Steel Frame Works" *Journal of Constructional Steel Research* vol. 27, pp. 3-21.

SIA Zürich (Société suisse des ingénieurs et des architectes) (2013). *SIA 263 Construction métallique.*

SZS (Centre Suisse de la construction métallique) (2005). C5/05 steelwork - *Tables de construction, Zürich: Centre suisse de la construction métallique.*

Taras A., Greiner R. , Unterweger H. (2013). "Proposal for amended rules for member buckling and semi-compact cross-section design - AM-1-1-2012-01 to 05." *Contribution to CEN TC 250 - SC3 – Eurocode 3 - Design of Steel Structures.*

Torabian S., Schafer B. (2013). "Strain capacity of cross-section elements and the role of local slenderness in the rotation capacity of structural steel." *Proceedings of the Annual Stability Conference, Structural Stability Research Council,* St. Louis, Missouri, pp. 450-470.